Zhao *et al.*
Chinese Journal of Mechanical Engineering (2022) 35:140
https://doi.org/10.1186/s10033-022-00807-z

Chinese Journal of Mechanical Engineering

ORIGINAL ARTICLE

Open Access

Microstructure and Mechanical Properties of Nickel-Aluminum Bronze Coating on 17-4PH Stainless Steel by Laser Cladding

Lu Zhao[1,2], Baorui Du[1], Jun Yao[1], Haitao Chen[3], Ruochen Ding[4] and Kailun Li[1*]

Abstract

Bimetallic copper-steel composite could be an effective structural material to improve the performance of traditional nickel-aluminum bronze (NAB) ship propeller due to its high structural strength and corrosion resistance. In this work, the defect-free NAB coatings has been successfully fabricated by laser direct depositing technique on the 17-4PH stainless steel substrate. The phase constitution, microstructure characteristics and hardness properties were investigated in details. The XRD results showed that the coatings mainly consisted of α-Cu, Fe and intermetallic κ phases despite the diffraction peaks shifted more than 0.5°, which may due to the influence of the Ni, Fe and Al atoms dissolved into Cu-matrix. The microstructures of the coatings were affected significantly by laser energy density according to SEM and EDS results. The top region of the coating was more undercooled during solidification, therefore the grains at this region was much finer than that at the bottom region. The higher energy input would lead to coarser grains. Fe-rich dendrites and spherical particles were found in the Cu matrix, which could be a result of liquid separation. The hardness of the coating is in the range of 204 $HV_{0.2}$–266 $HV_{0.2}$ which is higher than traditional as- cast NAB. The uneven distribution of Fe-rich phases as well as the hard κ phases could be the main reasons for the fluctuations of the hardness value. Tensile fracture occurred at bronze side, not at transition zone, which shows there is a good interfacial bonding between the two metals produced by laser cladding.

Keywords: Laser direct depositing, Nickel-aluminum bronze, Microstructure, Hardness, Tensile, Liquid separation

1 Introduction

Nickel-aluminum bronze (NAB) was developed for ship propellers and was widely used in valves and other marine industry parts due to its excellent mechanical properties and good corrosion resistance in sea water [1–5]. With the development of modern ships, the traditional NAB propeller has to be designed larger and heavier to ensure the strength, thus increases its manufacturing difficulty. Many kinds of steels have better strength and toughness than copper alloys, but the corrosion resistance of most stainless steels are lower. A novel composite structure of steel-based substrate with copper alloy cladded surface can reduce the difficulty of casting bronze parts in great thickness, maintain the original corrosion resistance as well as giving the structural strength provided by the steel substrate.

Steel-copper composite has been widely used but it is challenging to obtain the high bonding strength of the bimetallic structure. Smelting casting, diffusion welding and explosive welding could be used to produce copper layer on steel, but these techniques were limited by their low ability to form complex shapes [6–8]. A copper-silver alloy coating with the copper fraction of 59 ± 2 wt.% was produced on stainless steel by electroplating [9]. Cold – spray technique was employed to fabricate copper coatings on SS316L steel [10] where the nickel intermediate layer made good effects on the adhesion and deformation

*Correspondence: likailun@iet.cn

[1] Institute of Engineering Thermophysics, Chinese Academy of Sciences, Beijing 100190, China
Full list of author information is available at the end of the article

mechanisms at the interface. However, both of the methods could not obtain good metallurgical bonding between metals. Gas tungsten arc welding, laser melting and laser-arc hybrid welding methods were adopted for stainless steel and copper dissimilar joints [11–13]. The quantity of fused copper should be restricted in consideration of the influence of excess copper melting that may induce liquid separation and microcrack formation inside the fusion zone. The special design of the weld joint was the crucial step for traditional welds.

Laser direct depositing (LDD) is an effective additive manufacturing (AM) method to obtain net or near-net-shaped steel-copper composite parts. Many researchers have used this technique to fabricate coatings [14–18]. The effect of heat input via LDD on NAB was studied by Hyatt. The as-deposited material at its lowest heat input 42.5 J/mm was composed of entirely martensitic phase. As the heat input increases, the fraction of α phase increases. In particular, the hardness of the deposited material reaches the maximum value at the heat input of 64 J/mm, which may be due to the secondary precipitation-hardening [19]. Murray et al. fabricated near dense NAB part successfully via selective laser melting (SLM) technique with the lowest porosity of 0.05% ± 0.01%. The chemical composition analysis of as-fabricated NAB indicated a light loss of Fe and enrichment of Al, Ni and Mg [20]. Wire-arc additive manufacturing (WAAM) and heat-treatment were adopted on NAB to tuning the precipitation of κ-phases, and to adjust the mechanical properties and corrosion performance in turn. The thermal history of WAAM is similar to casting due to the large heat input of wire-arc and cyclic heating, so that the as- deposited phases are similar to the as- cast except the little β phases [21].

Most of the former works on AM of NAB focused on the forming process of single NAB material, but little studies on bimetallic steel-bronze structure and mechanical properties. This paper aims to obtain a steel-bronze composite structure by depositing NAB cladding layer on 17-4PH steel, and the microstructure together with mechanical properties are studied in details.

2 Materials and Methods

2.1 Materials

17-4PH stainless steel was chosen as the substrate material. The substrate prepared in size of 100 mm × 100 mm × 20 mm was solid solution treated. It was mechanically ground and cleaned with acetone and anhydrous ethanol. Spherical NAB powder particles with the diameter of 45–100 μm were selected in this experiment to ensure the uniformity and synchronicity of powder feeding. The morphology of NAB powder is shown in Figure 1. The powder was dried at 60 ℃ for 2 h. The chemical compositions of substrate and powder are listed in Table 1.

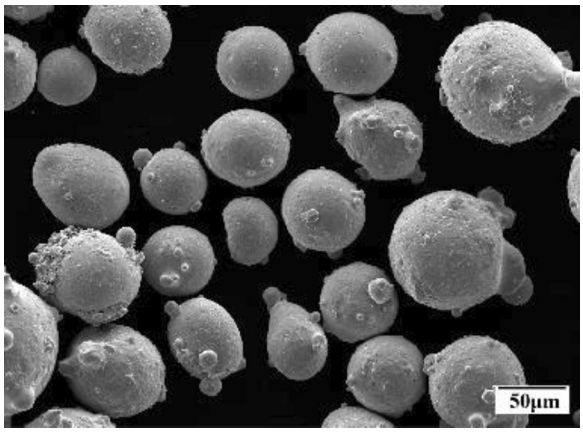

Figure 1 SEM image showing the morphology of NAB powder

2.2 Laser Processing

The LDD system was made up of an optical fiber laser (TRUMPF TruDiode 3006) in a continuous mode with a maximum power of 3000 W and the spot diameter of 3.4 mm, a NC precision machine, a powder feeder and a gas protection device (Figure 2). During executing process, laser beam, powder feeder and NC program were started up simultaneously, and the molten pool was protected from oxidation and pollution by a special nozzle blowing Ar gas to the melt surface directly at a rate of 10 L/min.

To study the influence of different process parameters on depositing quality, laser power was specified as processing variable, while the scanning speed and hatch distance were set as 1.2 m/min and 1.7 mm, respectively, and the laser repetition width rate was 50%. The power density transferred to energy density expression is as follows:

Table 1 Chemical composition of alloys

Material	Form	Element (wt.%)										
		Cu	Fe	Ni	Al	O	C	Si	Mn	P	S	Cr
17-4PH	Plate	3.230	Balance	4.040	–	–	0.044	0.440	0.660	0.027	0.003	15.600
CuAlNiFe	Powder	Balance	4.10	4.73	10.80	0.025	–	–	–	–	–	

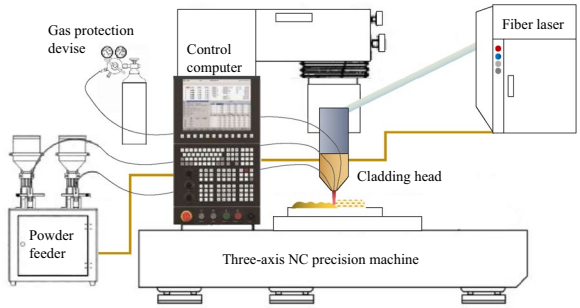

Figure 2 Schematic diagram of experiment apparatus for depositing

$$ED_V = \frac{P}{vht}, \tag{1}$$

where P is laser power, v is scanning speed, h is hatch distance and t is the thickness of the powder. The laser cladding parameters for each sample are presented in Table 2.

2.3 Material Characterization

A penetration test was taken to detect the surface defects. The penetrant was sprayed on the cladding surface and then penetrated into the defects through capillary force. The developer was sprayed on the surface after cleaning, and the penetrant at the defect would be sucked out and extended to the surface if flaws existed.

To examine the microstructure of the NAB coating, samples were cut into cuboid with the size of 10 mm × 10 mm × 7 mm. Metallographic preparation on cross-section was as follows: grinding on 400, 800, 1200, 1500 and 2000 # SiC paper in turn, polishing with diamond suspensions (3 μm and 1 μm), and etched by a metallographic etchant composed of 5 g $FeCl_3$ +20 mL HCl+100 mL H_2O. Leica DM1 5000M optical microscope (OM) was used to observe the microstructure of the cladding cross section. XRD analysis was performed on a Bruker D8 Advance X-ray diffractometer to determine the phases in the coatings. The diffractometer worked with Cu K_α radiation ($\lambda = 0.1540598$ nm) at 40 kV and 40 mA, and scans were performed over a 2θ range of 10°–100° with increments of 0.1° and step time of 2 s.

The surface morphology of the cross section was characterized using a TEMSCAN MIRA 3LMH scanning electron microscope (SEM) fitted with an Oxford energy dispersive spectrometer (EDS). Backscattered electron imaging (BSE) was carried out to distinguish the surface topography and surface chemistry.

The hardness was tested at a Vickers hardness tester (Everone MH-5L) equipped with a diamond regular pyramid tip. The distribution of the hardness at the cross section was measured using the load of 200 N and dwell time of 5 s.

The tensile testing samples were cut along the longitudinal direction of the steel- bronze composite with the interface of steel and NAB coating located at the center of the samples. Samples were built with length of 10 mm and thickness of 1.4 mm. The test was performed with CMT 5305GL machine at room temperature with a load speed of 0.1 mm/min.

3 Results

3.1 Phase Composition of Laser Coating

The XRD profile of the NAB coatings shows very different peaks from the raw powder (Figure 3). The phases presented in the NAB coatings are α-Cu, which could be a solid solution of Cu, Ni, Al, Fe and Cr, and κ phases (intermetallic compounds such as FeAl, Fe3Al and AlNi), as well as Fe phase. However, in contrast to the data of JCPDS (Joint Committee Powder Diffraction Standards), almost all the diffraction peaks have shifted more than 0.5° from their inherent angular positions. The first two diffractions of Cu are 43.41 and 50.56 in 65-9743# card, respectively, but 42.90 and 49.82, actually.

3.2 Defects in NAB Coating

Figure 4 shows the top morphologies of the coatings before and after the penetrating inspection. This bimetallic structure was composited of two metals with different thermal expansion coefficients, so it's inclined to form flaws as a result of thermal stress. However, no dyeing

Table 2 Laser cladding parameters

Sample code	Laser power (W)	Energy density (J/mm^3)	Scanning speed (m/min)	Hatch distance (mm)	Layer numbers
S1	2400	14.12	1.2	1.7	1
S2	2100	12.35	1.2	1.7	1
S3	1800	10.58	1.2	1.7	1
S4	1500	8.82	1.2	1.7	1
S5	2400	14.12	1.2	1.7	4
S6	1500	8.82	1.2	1.7	4

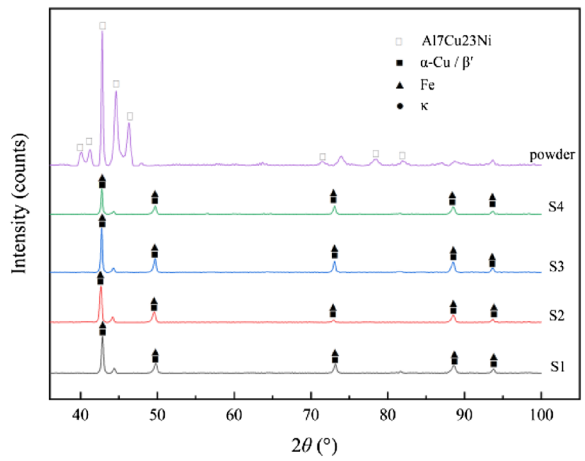

Figure 3 XRD patterns of laser depositing coatings

trace was detected after the penetrating, which illustrates no major pores or cracks were generated during the cladding process. Almost all composite parts bonded well except S4 (Figure 5). There is a hole defect with the about size of 40 μm.

3.3 Microstructure

Figure 6 shows the OM image of the cross section on S1. The coating consisted of three areas: bi-metal transition (zone 1), coarse grain zone combined with dark dendrites (zone 2) and acicular grain zone (zone 3).

Figure 7 shows the typical microstructure of S1. The matrix consisted of coarse grains accompanied with dark dendrites. The chemical compositions of the marked points in Figure 7 are listed in Table 3. It's obvious that the dendritic positions are rich in Fe and Cr, but poor in Cu and Ni. Combined with the XRD results, the light matrix is Cu-rich solid solution, and the dark dendrites are solidified phases of Fe-rich alloy in the coating (Figure 7a). As shown in Figure 7b, globular κ_{II} and lamellar κ_{III} precipitate on the boundary of α or β′ grains, and the other smaller dark particles could be designated as κ_{IV} according to Murray et al. [20]. Square 1–3# shows the different morphologies of Fe-rich dendrites.

Figure 8 shows the zone 1 and zone 3 of S1–S4. It can be seen that the microstructures are compact especially there is a good metallurgical bonding between coating and substrate. Thickness of transition zones are 5–14 μm. Light coarse grains and dark dendritic structures

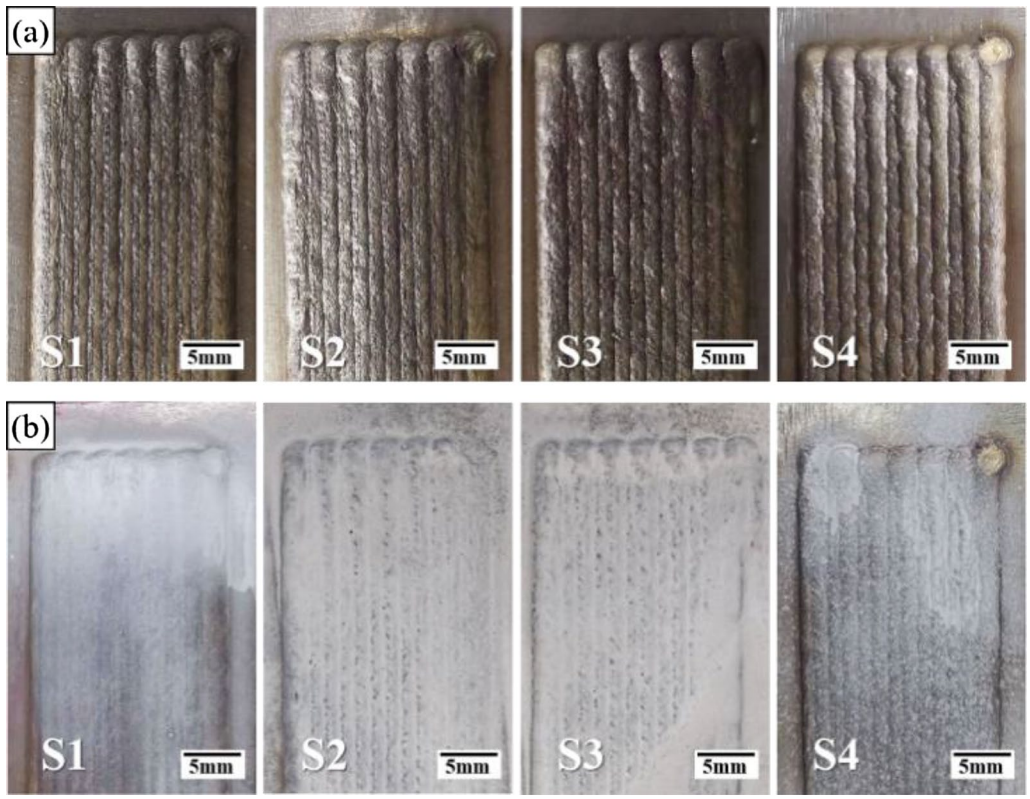

Figure 4 Top morphologies of cladding surfaces: **a** depositing surface and **b** HD-ST surface permeated by DPT-5 dyeing penetration

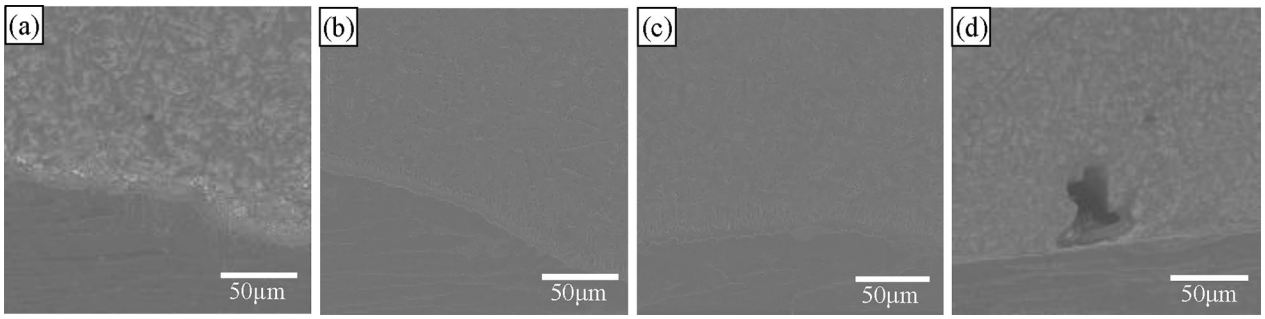

Figure 5 Section images of the interface area of **a** S1, **b** S2, **c** S3 and **d** S4

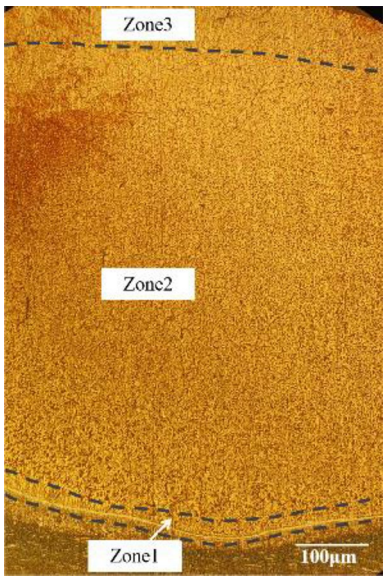

Figure 6 OM images of a metallographic specimen of the laser coating

are found in zone 1. The sizes of light grains are basically the same in each sample. The dark coarse dendrites embedded in the light grains. At the highest energy density of 14.12 J/mm^3, coarser grains and less fraction of needle-shaped dark phase (a, b) are formed compared to that of lower energy density at 12.35 J/mm^3 (c, d). All light grains are smaller in size and the fraction of secondary Widmanstatten structures are greater at 10.58 J/mm^3 (e, f) compared to the former cases. At the lowest energy density, more spiculate microstructures formed in zone 3 even in zone 1 (g, h).

The dendrite sizes range from a few microns to twenty microns (Figure 9). There are three types of spherical particles in the matrix, with diameters approximate of 3 μm, 1 μm and 0.1 μm, respectively, which are pointed out by the arrows. The spherical particles randomly distribute in the matrix, especially, some light finer spherical structures precipitate in the former larger dark ones that can be seen in 1#.

3.4 Mechanical Property

Figure 10 shows the hardness values of different samples at different positions. The result shows a general decreasing of hardness from the substrate to the coating and a sudden drop occurred at the transition zone. The hardness values of the coatings vary by a very small amount, which fluctuates between 204 $HV_{0.2}$ and 266 $HV_{0.2}$. There is no obvious relationship between the hardness and the energy input. Hardness depends on several factors such as grain size, phase type and phase content ratio. There were some abnormal values in the hardness curve, which were most possibly related to the uneven distribution of κ phases. When the κ phases are dense, the hardness is relatively high, and the hardness is relatively low where less κ phases are formed.

Figure 11 plotted the tensile stress-strain curves for S5 and S6. S5 is found to exhibit considerably longer elongation than S6. The ultimate tensile strength of S5 reached 767.80 MPa, and the specimen experienced ductile fracture. In light of the fracture occurred on the NAB body, it illustrated the interfacial strength was higher than that of as-deposited NAB. Micrographs of tensile fracture surfaces of composite structure are shown in Figure 12. Overall morphology of S5 seems cup like depression and a mass of dimples appears due to ductile fracture of the sample (Figure 12a, b). However, fracture surfaces of S6 show debonding at overlap on layer boundaries (Figure 12c, d).

4 Discussions

4.1 Evolution of the Unfused Defect

The dynamic of the molten pool under laser irradiation can be regarded as a flow process dominated by gravity, surface tension and capillary force. There is a significant competitive relationship between melt droplet wetting

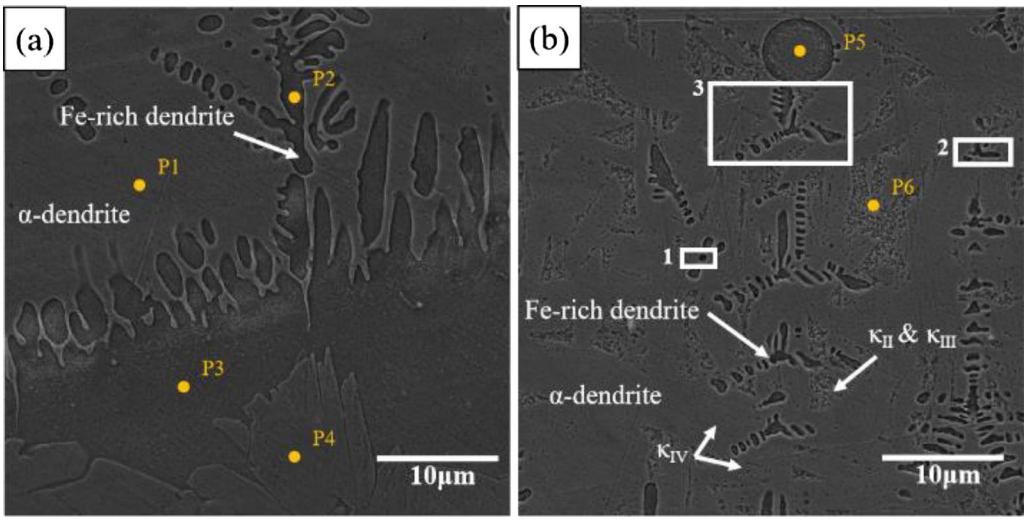

Figure 7 Typical microstructure of **a** zone 1 and **b** zone 2 of S1

Table 3 Element contents of cladding micro-zone (mass fraction, %)

Point	Cu	Fe	Cr	Ni	Al
1	85.0	3.0	0	5.0	7.0
2	21.9	56.1	10.9	5.5	5.6
3	6.3	71.1	17.2	4.0	1.4
4	5.4	74.0	16.9	3.8	0
5	13.9	61.5	15.8	4.6	4.3
6	75.8	4.3	0	9.5	10.4

(or spreading) and solidification process. As shown in Figure 5, unfused defects only occurred in S4. The lower laser energy density results in a lower molten temperature and stored energy. The surface tension of the melt at low temperature is higher, and the melt has poorer viscosity, spreadability and wettability. The low energy storage results in a faster solidification rate, that leading the melt droplets to solidify before they are fully spread. The melt droplet tends to form sphere spontaneously, causing balling on the laser scanning track, which generates the unfused defects in the local area of adjacent molten tracks [22, 23].

4.2 Account for the Shifts of XRD Peaks

Considerable shifts of most of the peaks reveal a rich solid solution relationship among Cu, Ni, Fe and Al elements. Such as an infinite solution between Ni and Cu, and a solid solubility of 9% for Al in Cu. According to Bragg's law (Eq. (2)), the degree of solid solution will cause the peak position (θ) shifts.

$$2d\sin\theta = n\lambda. \tag{2}$$

When a solid solution is formed, the dissimilar radius of the atom dissolved into the matrix, that can lead to the lattice distortion and enlarge the atomic radius of the solution. If the crystal plane spacing d increases, the θ value will decrease at a certain λ, showing the diffraction peak shifted to the left.

4.3 Microstructure Evolution

4.3.1 The Origin of Fe-rich Phases

Interestingly, the Fe-rich dendrites were found in the matrix of the coating. To further explore whether the Fe-rich dendrites in the coating were formed by a concentration of Fe element from the original powder, the multi-layer cladding test was carried out. Figure 13(a) shows the metallographic images of the cross section extracted from the S5 with multiple layers. As seen in Figure 13(b), layer 1 consists of large and light grains, dark and acicular structure and gray branched dendrites. The gray dendrites are Fe-rich phase, which have the same morphologies as those seen in Figure 8. The Fe-rich dendrites are absent in layer 2 (Figure 13(c)), which demonstrates that they are not originated from the powder but from the substrate.

The obvious spherical Fe-rich phase in the coating indicates the existence of liquid separation during solidificating. Laser cladding is a process of rapid solidification. When the laser energy density increases to 14.12 J/mm^3,

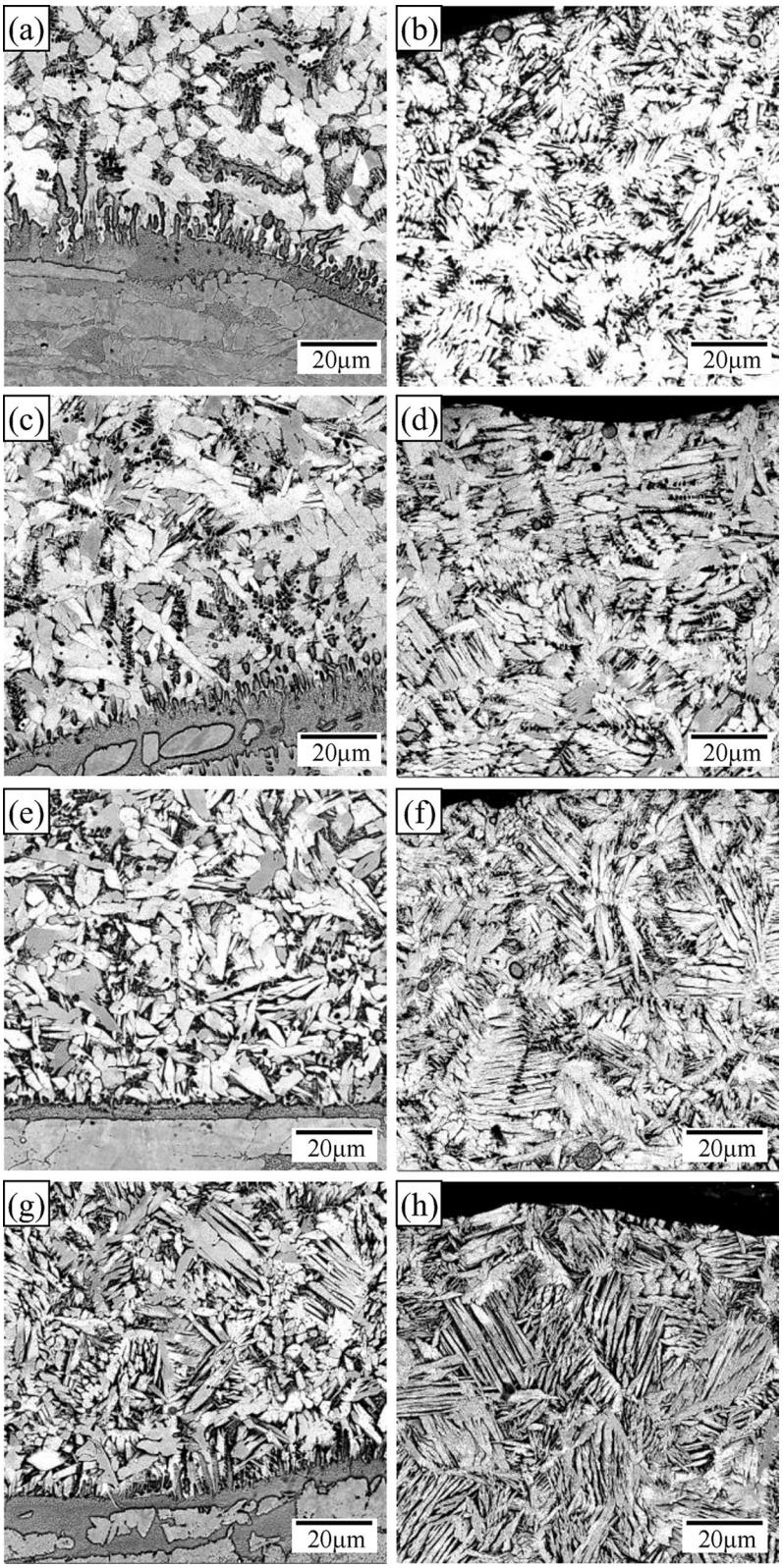

Figure 8 BSE images of laser depositing coatings: **a**, **b** zone 1 and zone 3 of S1; **c**, **d** zone 1 and zone 3 of S2; **e**, **f** zone 1 and zone 3 of S3; **g**, **h** zone 1 and zone 3 of S4

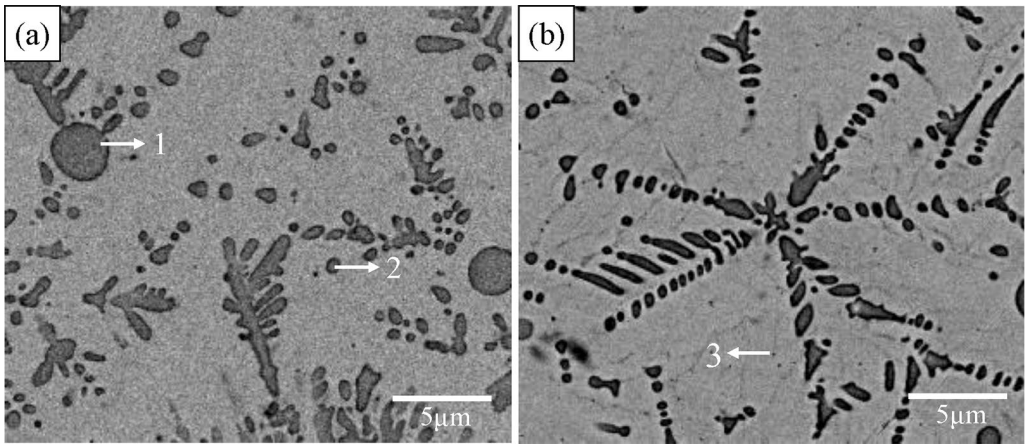

Figure 9 Typical dendritic structures in zone 2 of S2

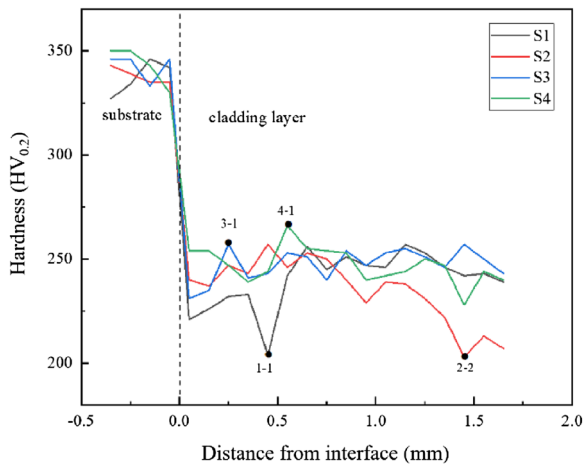

Figure 10 Distribution of hardness value along vertical section direction

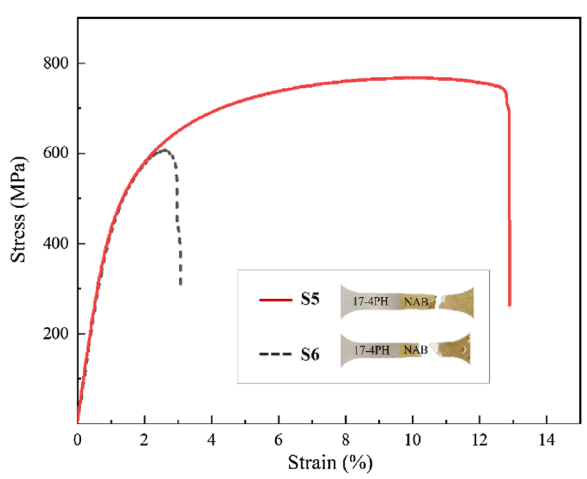

Figure 11 Tensile stress-strain curves for S5 and S6

the cooling rate could be more than 10^5 K/s due to the higher thermal conductivity than that of 316L steel [24]. Due to the intense convection and agitation in the molten pool, the Fe-based alloy floats through a buoyancy flow caused by density difference. Fe-rich droplets move up due to their lower density (7.8×10^3 kg/m^3) compared with that of copper-rich melts (8.5×10^3 kg/m^3). In the molten pool, the Fe-rich melt is wrapped by the copper-rich melt and contracted into a second spherical droplet due to the surface tension.

The solid solubility of Cu in iron is very low at room temperature (Figure 14), but Cu content in the spherical particles is up to 13.9% (Table 3). It indicates the spherical Fe-rich phase is a supersaturated solid solution containing Cu. The latent heat of crystallization releases during the solidification of Cu-rich melt causes the solidified Fe-rich dendrite to be remelted, which increases the temperature of the liquid phase and reduces the separation undercooling degree of the Fe-rich liquid. During the cooling process after rapid solidification, the secondary liquid phase separation occurs in the spherical Fe-rich particles, and a large number of fine Cu-rich grains are precipitated in the spherical Fe-rich particles. The larger the degree of undercooling is, the more obvious the liquid phase separates.

4.3.2 Microstructure Evolution in Local Regions

Since the thermal conductivity of NAB is higher than that of 17-4PH as well as the thickness of 17-4PH is nearly ten times thicker than that of NAB, the heat flux ratio of the cladding is much more than the substrate. At a certain energy input, most of the heat is emitted by the convective heat transfer between the coating and the air. At the interface, most of the heat is stored in the steel substrate. The heat transmits gradually through the coating, achieving a negative temperature

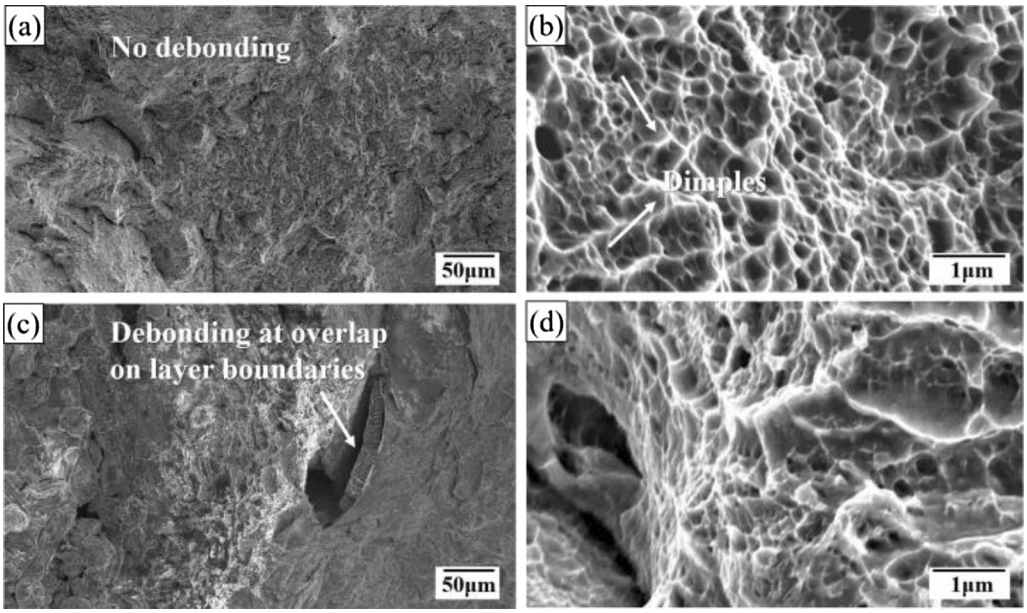

Figure 12 Tensile specimen and fracture surfaces after tensile testing: **a**, **b** S5; **c**, **d** S6

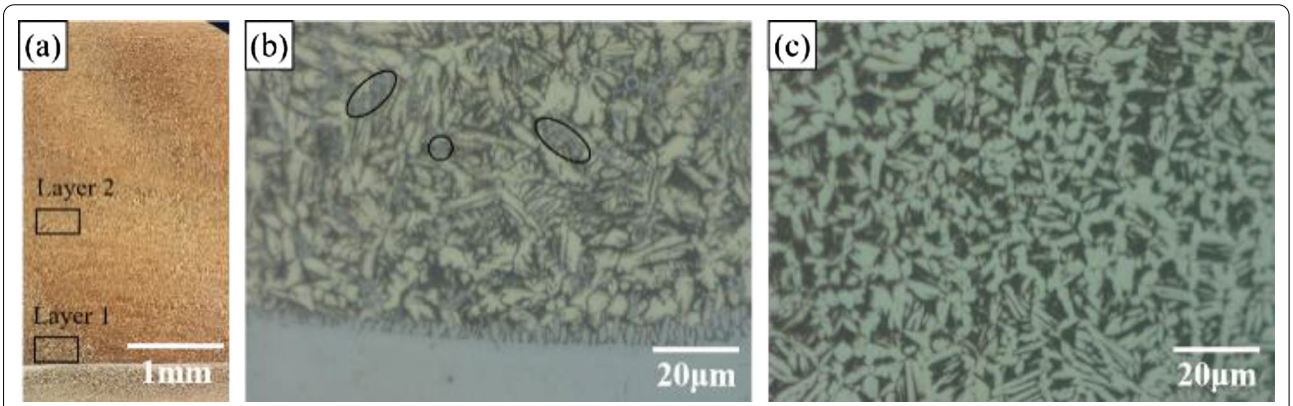

Figure 13 OM images of S5 section: **a** multi-layers; **b** layer 1; **c** layer 2

gradient G between the substrate and the molten pool. The inclined epitaxial growth was developed by the decreasing G/R values at the liquid-solid boundary while the initial G is large, and the simultaneous solidification speed of the cladding R is close to zero. Due to the high Fe liquidus temperature and the dominant Fe content at the fusion line, the Fe-rich melt solidified first, and then the Cu-rich melt begins to solidify around the Fe-rich phase. As it moves away from the molten pool boundary, the ratio of G/R also decreases while G decreases and R increases. When an occasional bulge occurs at the interface, it will continue to grow forward rapidly in contact with the melt with a greater degree of undercooling, which accelerate a condition for the growth of the columnar dendrites.

In the middle region of the cladding, the Fe-rich dendrites nucleate and develop in the melt. The evolution can be depicted in the marked 1–3# which represent different stages of growth (Figure 7). Simultaneously, heterogeneous nucleation and dendrite coarsening are dependent on the solidification time. The cooling rate and the degree of undercooling at the bottom of the coating are lower, so a long time of heat storage makes the α-Cu grains growing coarse.

In the upper region of the cladding, the large degree of undercooling caused by the heat exchange between the

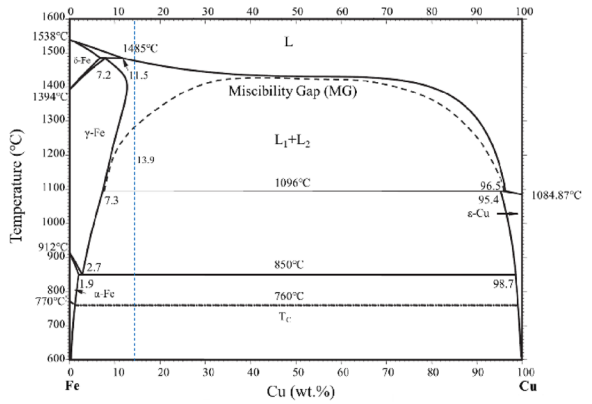

Figure 14 Cu-Fe binary phase diagram with metastable miscibility [25]

melt and the air provides the driving force for the phase transition, and the nucleation begins when the temperature decreases to the solidus line of the alloy. Since the interior melt is in an overheated state and the heat conduction direction is vertical outward from the top surface, the front of the solid-liquid interface has a positive temperature gradient. The crystal grows in a dendritic manner with the bulge accidentally formed entering the undercooled liquid, achieving a high growth rate and branching continuously to form a dendritic skeleton.

4.3.3 Effect of Laser Energy on Microstructure

During the laser cladding process, high energy beam melts the powder and substrate simultaneously. The dilution of substrate causes part of the steel mixed into the coating with the liquid fluid. The final chemical composition of the molten zone is related to the dilution degree of the substrate.

The solidification microstructure dimension of depositing materials is determined by the ratio of cooling rate GR. The secondary dendrite arm spacing of the columnar and equiaxed dendrites can reflect the dimension which is predicted in the following equation [26]:

$$d = at_f^n = b(\varepsilon_C)^{-n}, \tag{3}$$

where t_f is local solidification time, ε_C is cooling rate, and a, b and n are material specific constants. In the solidification process, a slower cooling rate and a longer coarsening time will develop coarser structures with a larger size of dendrite arms. Therefore, a higher laser energy density provides more energy stored in the composite structure which makes for structures coarsen.

4.4 Relationship of Mechanical Properties and Microstructure

Table 4 lists the chemical compositions of six types of NAB alloys. Compared to UNS C95500 alloy [22] and the UNS 95800 specimen cut from propeller blades [27], the hardness of the laser coatings is higher than NAB materials processed by the traditional method, but some abnormal values exist on points in Figure 10.

The mass transfer and composition mixing of the powder and substrate in the molten pool have an important effect on the hardness. In general, the hardness of α phase is low, that of β' phase is higher, and that of κ phase is the highest which concludes a series of Al(Fe, Ni) intermetallic compounds. There are three strengthening mechanisms that are solid solution strengthening, precipitation strengthening and dispersion strengthening, and one mechanism of weakening hardness, which is related closely to the hardness of copper alloy cladding layer. The solid solution elements such as Al and Ni are present in α phases, and these solute atoms hinder dislocation motion, that solid solution strengthening works. In addition, many spherical particles that without enough time to merge were acted as reinforcement phase embed in the matrix and prevent dislocation migration, resulting in the increase of hardness of the coating. Al, Ni and Fe form the κ phases with high hardness, which is dispersed in the coating matrix and make precipitation strengthening of the second phase [28, 29]. Appropriate amount of Fe and Ni added to the aluminum bronze alloy can refine the grain, and it is fine grain strengthening mechanism of improving the strength and hardness. Due to the dilution of the substrate, a large amount of Fe-Cr melt mixed into the molten pool and solidified into dendritic structures. As such points 1-1 and 2-2, the laser energy applied at these areas happens to be the higher power parameters, which led to a higher degree of dilution and introduces more Fe-rich melt into the coating. The iron dendrite phases were dense and developed in these regions, resulting in a low local hardness.

As can be seen, S5 has a good tensile property. However, the flat regions on S6 revealed the origin location of fracture. There is a possibility of unmelted powder on this laser parameter. Further, the next layer is deposited on the bumpy surface where there were low-lying areas left by the overlap that results in positive defocus of the laser. This situation provided insufficient laser energy density

Table 4 Hardness of UNS ASTM NAB and as-deposited NAB

Alloy	Condition	Hardness value	Vickers hardness
C95500	As-cast	190 HB	200 HV
Specimen cut from propeller blades (UNS designation 95800)	Heat-treated	159 $HV_{0.2}$	159 HV
S1	As-deposited	204 HV (minimum)	204 HV (minimum)
S2	As-deposited	204 HV (minimum)	204 HV (minimum)
S3	As-deposited	231 HV (minimum)	231 HV (minimum)
S4	As-deposited	228 HV (minimum)	228 HV (minimum)

on powder and would increase the range of uncompleted melt region.

5 Conclusions

This study presents the influence of four different laser conditions on the microstructure and mechanical properties of nickel aluminum bronze coatings. Following conclusions could be drawn.

1. A bimetallic steel and bronze structure with a good metallurgical bonding but without pores, cracks and other defects can be obtained by laser depositing.
2. The microstructure of NAB cladding was affected significantly by the laser thermal history. The grain size of the cladding near the interface is lager, and the grain shape inclined needle-like in the upper zone.
3. The hardness of NAB cladding was strongly dependent on the microstructure, especially on the mass fraction of Fe components, but not on the cooling rate. The value of cladding section was about 204 $HV_{0.2}$–266 $HV_{0.2}$. A large number of Fe -rich dendrites, hard κ phases and spherical Fe-rich particles produced by the liquid separation led to the fluctuation of hardness value.
4. Tensile testing of composite structure showed it fractured on bronze body but not the transition zone. The interface strength is higher than 767.80 MPa. The characteristic of ductile fracture revealed there was a good bonding performance between such two alloys by laser cladding.

Acknowledgements
Not applicable.

Author contributions
LZ was in charge of the whole trial and wrote the manuscript; BD conceived the study; JY, HC, RD and KL analyzed data; Additionally, KL contributed to the writing revisions. All authors read and approved the final manuscript.

Authors' Information
Lu Zhao, born in 1986, is currently a PhD candidate at *University of Chinese Academy of Sciences*, meanwhile, subject to *Institute of Engineering Thermophysics, Chinese Academy of Sciences*. She received her master degree from *Harbin Engineering University, China*, in 2012. Her research interests include laser additive manufacturing with metallic material and its application. Tel: +86-15942336608;
Baorui Du, born in 1970, is currently a researcher at *Institute of Engineering Thermophysics, Chinese Academy of Sciences*. He received his master degree from *Beihang University, China*, in 1999. His research interests include additive manufacturing with metallic material, numerical control machining technology and their applications in the field of aviation.
Jun Yao, born in 1988, is currently an engineer at *Institute of Engineering Thermophysics, Chinese Academy of Sciences*. He received his doctoral degree on mechanical manufacture and automation from *Beihang University, China*, in 2018.
Haitao Chen, born in 1975, is currently a senior engineer at *Shenyang Dalu Laser Advanced Manufacturing Technology Innovation Co. Ltd, China*. His research interests include laser additive manufacturing with metallic material and its application.
Ruochen Ding, born in 1992, is an engineer at *Institute of Science and Technology, China Three Gorges Corporation*. She received her doctoral degree on engineering thermophysics from *University of Chinese Academy of Sciences*, in 2021. E-mail: dingruochen@163.com.
Kailun Li, born in 1993, is currently an engineer at *Institute of Engineering Thermophysics, Chinese Academy of Sciences*. He received his doctoral degree on materials science and engineering from *Tsinghua University, China*, in 2020.

Funding
Not applicable.

Competing interests
The authors declare no competing financial interests.

Author Details
[1]Institute of Engineering Thermophysics, Chinese Academy of Sciences, Beijing 100190, China. [2]University of Chinese Academy of Sciences, Beijing 100049, China. [3]Shenyang Dalu Laser Advanced Manufacturing Technology Innovation Co. Ltd, Shenyang 110000, China. [4]Institute of Science and Technology, China Three Gorges Corporation, Beijing 100038, China.

Received: 18 August 2021 Revised: 25 March 2022 Accepted: 24 October 2022
Published online: 24 November 2022

References

[1] E A Culpan, G Rose. Microstructural characterization of cast nickel aluminium bronze. *Journal of Materials Science*, 1978, 13: 1647–1657.
[2] A Jahanafrooz, F Hasan, G W Lorimer, et al. Microstructural development in complex nickel aluminum bronzes. *Metallurgical Transactions A*, 1983, 14: 1951–1956.
[3] I Richardson. *Guide to nickel aluminium bronze for engineers*. USA: Copper Development Association, 2016.
[4] R Z Tian, Z T Wang. *Handbook of copper alloy and its processing*. Changsha: Central South University Press, 2007.

[5] M Hauer, F Gärtner, S Krebs, et al. Process selection for the fabrication of cavitation erosion-resistant bronze coatings by thermal and kinetic spraying in maritime applications. *Journal of Thermal Spray Technology*, 2021, 30: 1310–1328.
[6] L Dong, W Chen, L Hou, et al. Metallurgical process analysis and microstructure characterization of the bonding interface of QAl9-4 aluminum bronze and 304 stainless steel composite materials. *Journal of Materials Processing Technology*, 2016, 238: 325–332.
[7] S Sebastian, V Suyamburajan. Microstructural analysis of diffusion bonding on copper stainless steel. *Materials Today: Proceedings*, 2021, 37: 1706–1712.
[8] H Zhang, K Jiao, J Zhang, et al. Microstructure and mechanical properties investigations of copper-steel composite fabricated by explosive welding. *Materials Science & Engineering A*, 2018, 731: 278–287.
[9] N Ciacotich, R U Din, J J Sloth, et al. An electroplated copper–silver alloy as antibacterial coating on stainless steel. *Surface & Coatings Technology*, 2018, 345: 96–104.
[10] S Singh, H Singh. Effect of electroplated interlayers on bonding mechanism of cold-sprayed copper on SS316L steel substrate. *Vacuum*, 2020, 172: 109092.
[11] Y Poo-arporn, S Duangnil, D Bamrungkoh, et al. Gas tungsten arc welding of copper to stainless steel for ultra-high vacuum applications. *Journal of Materials Processing Technology*, 2020, 277: 116490.
[12] S Chen, J Huang, J Xia, et al. Microstructural characteristics of a stainless steel/copper dissimilar joint made by laser welding. *Metallurgical and Materials Transactions A*, 2013, 44: 3690–3696.
[13] Y Meng, X Li, M Gao, et al. Microstructures and mechanical properties of laser-arc hybrid welded dissimilar pure copper to stainless steel. *Optics and Laser Technology*, 2019, 111: 140–145.
[14] Y Li, S Dong, P He, et al. Microstructure characteristics and mechanical properties of new-type FeNiCr laser cladding alloy coating on nodular cast iron. *Journal of Materials Processing Technology*, 2019, 269: 163–171.
[15] J Liu, H Liu, X Tian, et al. Microstructural evolution and corrosion properties of Ni-based alloy coatings fabricated by multi-layer laser cladding on cast iron. *Journal of Alloys and Compounds*, 2020, 822: 153708.
[16] S Singh, M Kumar, G P S Sodhi, et al. Development of thick copper claddings on SS316L steel for In-vessel components of fusion reactors and copper-cast iron canisters. *Fusion Engineering and Design*, 2018, 128: 126–137.
[17] Y Zou, B Ma, H Cui, et al. Microstructure, wear, and oxidation resistance of nanostructured Microstructure, wear, and oxidation resistance of nanostructured carbide-strengthened cobalt-based composite coatings on Invar alloys by laser cladding. *Surface & Coatings Technology*, 2020, 381: 125188.
[18] L Zhu, Y Liu, Z Li, et al. Microstructure and properties of Cu-Ti-Ni composite coatings on gray cast iron fabricated by laser cladding. *Optics and Laser Technology*, 2020, 122: 105879.
[19] C V Hyatt, K H Magee, T Betancourt. The effect of heat input on the microstructure and properties of nickel aluminum bronze laser clad with a consumable of composition Cu-9.0Al-4.6Ni-3.9Fe-1.2Mn. *Metallurgical and Materials Transactions A*, 1998, 29: 1677–1690.
[20] T Murray, S Thomas, Y Wu, et al. Selective laser melting of nickel aluminium bronze. *Additive Manufacturing*, 2020, 33: 101122.
[21] C Dharmendra, B S Amirkhiz, A Lloyd, et al. Wire-arc additive manufactured nickel aluminum bronze with enhanced mechanical properties using heat treatments cycles. *Additive Manufacturing*, 2020, 36: 101510.
[22] ASTM. *Standard specification for aluminum-bronze sand castings*. USA: ASTM B148-2014, 2014.
[23] X Zhou, X Liu, D Zhang, et al. Balling phenomena in selective laser melted tungsten. *Journal of Materials Processing Technology*, 2015, 222: 33–42.
[24] M Ma, Z Wang, X Zeng. A comparison on metallurgical behaviors of 316L stainless steel by selective laser melting and laser cladding deposition. *Materials Science & Engineering A*, 2017, 685: 265–273.
[25] H Okamoto. Supplemental literature review of binary phase diagrams: Au-Dy, Au-Sc, Au-Yb, C-Hf, C-Ta, Cu-Fe, Dy-Mn, Er-Mn, Ho-Mn, Mn-Tb, Mn-Tm, and Sb-Sn. *Journal of Phase Equilibria and Diffusion*, 2017, 38: 160–170.
[26] S Kou. *Welding metallurgy*. New Jersey: John Wiley & Sons, Inc., 2003.
[27] C H Tang, F T Cheng, H C Man. Improvement in cavitation erosion resistance of a copper-based propeller alloy by laser surface melting. *Surface and Coatings Technology*, 2004, 182: 300–307.
[28] Y Li, Y Lian, Y Sun. Cavitation erosion behavior of friction stir processed nickel aluminum bronze. *Journal of Alloys and Compounds*, 2019, 795: 233–240.
[29] Y Zeng, F Yang, Z Chen, et al. Enhancing mechanical properties and corrosion resistance of nickel-aluminum bronze via hot rolling process. *Journal of Materials Science & Technology*, 2021, 61: 186–196.